

Chemistry in a cryogenic buffer gas cell

Qi Sun,^{1,*} Jinyu Dai,^{1,*} Rian Koots,² Benjamin Riley,¹ Jesús Pérez-Ríos,² Debayan Mitra,^{1,3,†} and Tanya Zelevinsky^{1,‡}

¹*Department of Physics, Columbia University, New York, NY 10027, USA*

²*Department of Physics and Astronomy, Stony Brook University, Stony Brook, New York, NY 11794, USA*

³*Department of Physics, Indiana University, Bloomington, IN 47405, USA*

(Dated: January 13, 2025)

Cryogenic buffer gas sources are ubiquitous for producing cold, collimated molecular beams for quantum science, chemistry, and precision measurements. The molecules are typically produced by laser ablating a metal target in the presence of a donor gas, where the radical of interest emerges among the reaction products due to a barrier-free process or under thermal or optical excitation. High-barrier reactions, such as between calcium and molecular hydrogen, should be precluded. Here, we study chemical reactions between Ca and three hydrogen isotopologues H₂, D₂, and HD in a cryogenic cell with helium buffer gas. Remarkably, we observe that H₂ can serve as both a reactant and a buffer gas, far outperforming D₂ and HD. Our results demonstrate a robust method for generating cold beams of alkaline-earth-metal hydrides for laser cooling and trapping. The observations are complemented by a reaction model, yielding qualitative agreement with the experiment.

I. INTRODUCTION

Chemical reactions at low densities and low relative energies are characterized by the limited number of available reactive trajectories. Such reactions occur in astrophysical environments and may be responsible for the production of hydrocarbons in the early universe [1, 2]. Studies of rate coefficients for single-collision events in controlled laboratory environments can shed light on phenomena such as quantum interference between reaction pathways [3, 4] and the role of entanglement in reactions [5]. Techniques such as cold molecular beams [6, 7], supersonic jets [8–10], Stark deceleration [11, 12], centrifuge deceleration [13], ion trapping [14–18], optical lattice trapping [19], and optical tweezers [20] have enabled extreme reaction regimes unrealizable with traditional techniques and have exposed new quantum phenomena [21].

However, there is an intermediate regime in the chemical reaction landscape where densities and temperatures straddle the line between quantum and classical [22]. Here, the motional states of the reactants can be treated classically but the quantum nature of their internal states cannot be neglected. This regime is manifested in cryogenic buffer gas beam (CBGB) sources [23, 24]. Typical gas densities in a CBGB source can be of the order of 10^{15} cm⁻³ and equilibrium temperatures of the order of 4 K. But laser ablation, which is typically used to create the molecules of interest, can produce transient temperatures as high as 10^4 K [25]. Hence this configuration allows scattering processes that extend from multiple partial waves [26, 27] to simple hard-sphere scattering [28]. CBGB sources are experimentally versatile since different gaseous reactants can be introduced with ease. Therefore, a CBGB source is an ideal playground to study chemistry over a large parameter range.

Three physical and chemical processes occur in a CBGB source. The first one consists of elastic collisions between

the cold buffer gas and particles of interest, leading to translational cooling. The second one is inelastic collisions that reduce the internal temperature, or ro-vibrational cooling. The third one is chemical reactions that actually produce the particles of interest. The combination of the first two processes is buffer gas cooling, which has been a very successful technique for producing cold beams of atoms and molecules in their ro-vibrational ground states [24]. The third, reactive process has attracted renewed attention since many new molecular species have been successfully produced in CBGBs. These molecules range from diatomics such as CaF [29], YbF [30] and AlF [31, 32], to triatomics such as CaOH [33], YbOH [34] and SrOH [35], to polyatomics such as CaOCH₃ [36] and CaOC₆H₅ [37]. The typical protocol to produce a molecule of type *MX* is to laser ablate a metal target ($M = \text{Ca, Sr, Yb, } \dots$) and allow the resulting hot plume to react with a donor gas ($RX = \text{SF}_6, \text{H}_2\text{O, CH}_3\text{OH, } \dots$).

Typical reactions in CBGB sources are either barrierless or have low barriers that can be overcome with thermal or optical excitation. For example, Ca and SF₆ exothermically react to produce CaF [38], while the reaction between Ca and H₂O to produce CaOH requires exciting the Ca atom to the metastable ³P₁ state to overcome the ~ 1.3 eV barrier [33]. In contrast, the reaction between Ca and H₂ has a barrier of ~ 2.7 eV. Temperatures as high as $\sim 3 \times 10^4$ K would be required to overcome this barrier thermally, which is not readily accessible with laser ablation. One might expect such a reaction to produce a very low yield. In this work, we study the reaction of Ca atoms with H₂, D₂, and HD isotopologues, both with and without helium as a buffer gas. Counterintuitively, we find that the reaction is far more efficient than could be expected from a simple thermodynamic estimate, pointing to the critical role of the reaction dynamics over pure energetic considerations. Furthermore, we find that H₂, but not D₂ or HD, can serve as a buffer gas and thermalize the resulting CaH molecules to their ro-vibrational ground state. To explain these results, we model the reactant dynamics using rates obtained from quasi-classical trajectory simulations (QCT). Our calculations elucidate the general trends observed in the experiment and provide an order-of-magnitude estimate of reaction rates.

* These authors contributed equally to this work

† debayanm@iu.edu

‡ tanya.zelevinsky@columbia.edu

II. EXPERIMENTAL IMPLEMENTATION

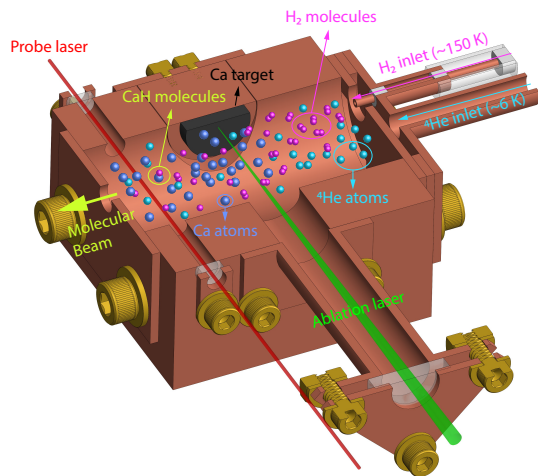


FIG. 1. Horizontal cross section of the cryogenic buffer gas cell. Hot Ca atoms are generated via laser ablation of a solid target and subsequently react with H_2 molecules that flow in at ~ 150 K. Additionally, ^4He flows in at ~ 6 K for efficient buffer gas cooling. The Ca atoms and the product molecules are probed through laser absorption, with optical access ~ 2 cm downstream from the target.

Figure 1 illustrates the experimental setup. A copper cell with inner dimensions of 25.4 mm in diameter and 50.8 mm in length is thermally anchored to a pulse tube refrigerator cold plate at ~ 6 K. A Ca metal target is attached to the cell. We employ a pulsed Nd:YAG laser at 532 nm, focused onto the Ca target with a beam diameter of ~ 100 μm , to ablate the target with an energy of up to ~ 30 mJ per pulse, pulse duration of ~ 10 ns, and repetition rate of ~ 1 Hz, creating a hot plume of Ca atoms. We simultaneously flow multiple species of gas into the cell for chemical reactions and thermalization. A thermally isolated fill line held at ~ 150 K is attached to the cell to flow H_2 , D_2 and HD . He gas is pre-cooled to ~ 6 K and diffused so the distribution inside the cell is homogeneous for more effective cooling. We probe the atoms and molecules of interest through laser absorption, via optical access ~ 2 cm downstream from the target. Specifically, we probe Ca atoms on the $4s4p\ ^3P_1 \leftarrow 4s^2\ ^1S_0$ transition at 657 nm and CaH molecules on the $A^2\Pi_{1/2}(v' = 0, J' = 3/2, +) \leftarrow X^2\Sigma^+(v'' = 0, N'' = 1, J'' = 1/2, -)$ transition at 695 nm. We convert the CaH molecular density in the $X^2\Sigma^+(v = 0, N = 1, J = 1/2, -)$ state to cover all ro-vibrational states up to $(v = 0, N = 2)$, accounting for all the cold molecules generated (Appendix A).

III. RESULTS

A. Ca + H_2 chemical reaction in a CBGB source

Due to its endothermic nature, the Ca + H_2 chemical reaction is expected to be barely within reach in a CBGB source.

However, we observe substantial production ($\sim 3\text{-}10 \times 10^{10}$ molecules/steradian/pulse) of CaH molecules due to unique properties of cryogenic H_2 , as explained below. We carefully calibrate the internal state distribution at various ablation energies up to the highest occupied state ($v = 0, N = 2$) (Appendix A). We conclude the total CaH density in these internal states represents the entire CaH yield. The reaction occurs starting from the H_2 flow of a few standard cubic centimeters per minute (1 SCCM $\approx 4.5 \times 10^{17}$ molecules per second), and saturates at several tens of SCCM. This process is $\sim 2\text{-}3$ orders of magnitude more efficient than the exothermic reactions with other hydrogen isotopologues that we investigated; we further find that H_2 can serve as buffer gas without the need to flow He (Section III B).

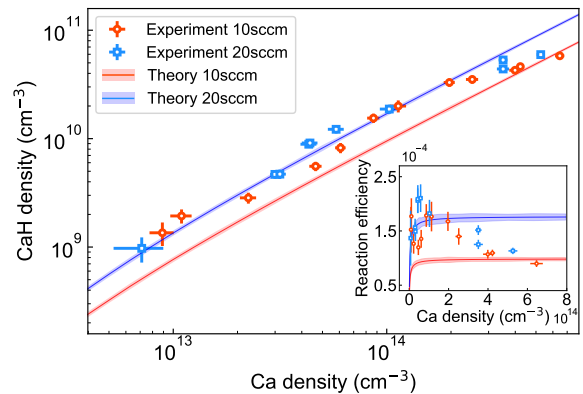


FIG. 2. Chemical reaction in a cryogenic buffer gas cell. Time-averaged CaH density measurements (0-1 ms after ablation) as a function of Ca density, for 10 SCCM of H_2 (red points) and 20 SCCM of H_2 (blue points). The lines denote theoretical results at the same conditions, showing qualitative agreement. The inset shows reaction efficiency, defined as the ratio of CaH and Ca densities. A notable decrease in reaction efficiency is observed experimentally at higher Ca densities, whereas the theoretical model does not capture this trend, showing the need for further refinement. Experimental data points include 1- σ statistical errors.

Figure 2 shows the total measured CaH density as a function of the initial Ca density. The Ca density is varied by adjusting the ablation energy, which can also alter the ablation plume temperature. We develop a chemical reaction network model (lines in Fig. 2), utilizing the rates from QCT calculations (Appendix B). We find that a constant plume temperature with respect to Ca density provides the best fit to the data. This assumption is tested by measuring the plume temperature without gas flow (Appendix C). We find a maximum 45(10)% increase with ablation energy, supporting the constant temperature assumption.

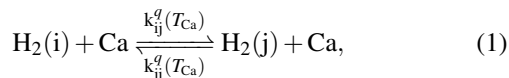
While the data is in reasonable agreement with the reaction model predictions, some discrepancies arise at high Ca densities. As shown in the inset of Fig. 2, the reaction efficiency, or the fraction of Ca atoms converted to CaH molecules, falls toward higher densities. In contrast, in the reaction model the reaction efficiency saturates at high densities. This may be because the model does not include diffusion dynamics or non-equilibrium processes. One possibility is that the cool-

ing is accelerated at higher densities, lowering the final CaH yield.

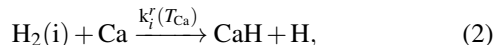
1. Reaction network model

The reaction model considers collisions between the ablated Ca atoms and H₂ molecules, allowing for vibrational excitation of H₂ and formation of CaH. We find that the vibrational state of H₂ affects the reaction while the rotational state does not. Thus we assume H₂ to be in the rotational ground state.

The cold H₂ gas in the CBGB source is assumed to be in the ground vibrational state initially. The model includes inelastic vibrational transitions of H₂ due to collisions with Ca in the cell,



where $i = (0, 1)$, $j = (1, 2)$, $i \neq j$ represent the vibrational level of the molecule. The formation of CaH is described as



where $i = (0, 1, 2)$ represents the vibrational level of H₂. Each collision has an associated temperature-dependent rate which is calculated via the QCT method (Appendix B), $k_{ij}^q(T_{\text{Ca}})$ for the vibrational excitation of H₂ and $k_i^r(T_{\text{Ca}})$ for the formation of CaH.

We use a deterministic approach to study the evolution of these reactions in a closed system at thermal equilibrium by solving the set of differential equations associated with Eqs. (1) and (2). The temperature of the reaction is given by the translational temperature of Ca, or T_{Ca} , which falls via collisions with the H₂ and He buffer gases according to

$$\frac{dT_{\text{Ca}}}{dt} = -\frac{R_{\text{H}_2}(T_{\text{Ca},0} - T_{\text{H}_2})}{\kappa_{\text{H}_2}} - \frac{R_{\text{He}}(T_{\text{Ca},0} - T_{\text{He}})}{\kappa_{\text{He}}}. \quad (3)$$

The elastic collision rate between Ca and buffer gas (BG = He, H₂) is given by $R_{\text{BG}} = n_{\text{BG}}\sigma_{\text{BG}}^{\text{el}}\bar{v}_{\text{BG}}$, where n_{BG} , $\sigma_{\text{BG}}^{\text{el}}$, and \bar{v}_{BG} are the BG density, elastic cross section between Ca and BG, and average relative velocity between Ca and BG, respectively. $T_{\text{Ca},0}$ is the initial kinetic temperature of Ca, and $\kappa_{\text{BG}} \equiv (m_{\text{Ca}} + m_{\text{BG}})^2 / (2m_{\text{Ca}}m_{\text{BG}})$. More details of the reaction network model and QCT methods can be found in Appendix B and Ref. [39].

B. H₂ as a buffer gas coolant

We observe a pronounced discrepancy in the experimental production of CaH or CaD depending on whether H₂, HD, or D₂ is used as the reactant gas. With H₂, substantial yields of thermalized Ca atoms and CaH molecules are detected, even in the absence of He as a buffer gas (Fig. 3, green). In contrast, using HD or D₂ under similar conditions results in significantly lower yields of thermalized Ca atoms, with molecular

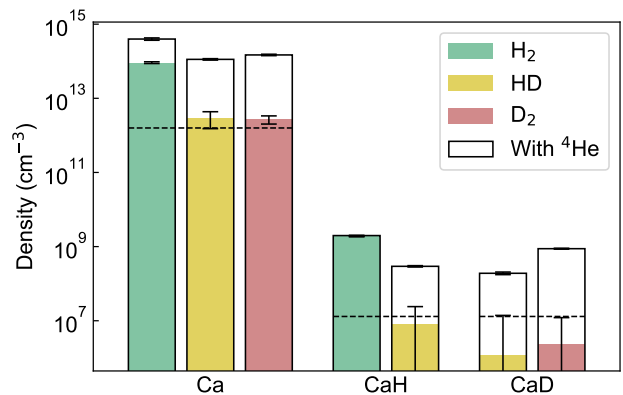


FIG. 3. Time-averaged densities (0-1 ms after ablation) of Ca and CaH (or CaD) under different gas flow configurations. Reactant gases H₂, HD, or D₂ are supplied at 20 SCCM, with He (if used) added at 8.8 SCCM. Ablation energy is 19 mJ per pulse. Green, yellow, and red bars represent results for H₂, HD, and D₂, respectively, while black-framed bars show the yields with He added. The dashed lines indicate the detection limits.

production falling below our detection limits (Fig. 3, yellow and red). These findings highlight the unique advantages of H₂ as a reactant and cooling medium in CBGB systems.

This phenomenon can be explained by the exceptionally high saturated vapor pressure of H₂ at cryogenic temperatures. For instance, the vapor pressure of H₂ at 6 K is ~ 1.5 mTorr, a few orders of magnitude higher than for HD (4.0×10^{-2} mTorr) and D₂ (1.5×10^{-3} mTorr) [40, 41]. This high vapor pressure allows a sufficient density of H₂ molecules to remain in the gas phase, enabling several productive collisions with Ca atoms before adhering to the cell walls or exiting the cell, and thus facilitating efficient chemical reactions and thermalization. In contrast, the lower vapor pressures of HD and D₂ result in rapid conversion to a condensed phase, leaving an insufficient gas-phase density to sustain a reaction with Ca. Additionally, the QCT simulations indicate an order of magnitude decrease in the formation of CaD in the presence of D₂ when compared with CaH formation in the presence of H₂. This can be attributed to the increased mass of D₂ compared with H₂ [39].

Introducing cryogenic He into the system enhances the yields of both thermalized Ca atoms and CaH molecules across all reactants (black-framed bars in Fig. 3). This effect is likely due to He's high efficiency in gas mixture thermalization and providing hydrodynamic entrainment [24], which helps maintain a more stable and homogeneous environment in the cryogenic cell that is conducive to Ca and CaH detection. Adding He into the system therefore mitigates the limitations imposed by the lower vapor pressures of HD and D₂. Note that the CaH molecular yield does not increase as much as the thermalized Ca yield in the presence of He. This could be attributed to a faster drop of the Ca atom temperature in the presence of cryogenic He which in turn reduces the chemical reaction efficiency.

C. Collisional cross sections

Elastic collisions play a pivotal role in the thermalization process of CBGB systems. Larger elastic cross sections correspond to higher collision rates, facilitating rapid thermal equilibration of translational degrees of freedom. Inert gases such as He and Ne are often favored as buffer gas choices due to their relatively large elastic collisional cross sections with a variety of molecular species, on the order of 10^{-14} cm². Due to our observations of a strong H₂ buffer gas cooling effect, here we study the elastic cross sections of H₂, HD, and D₂ with Ca and CaH.

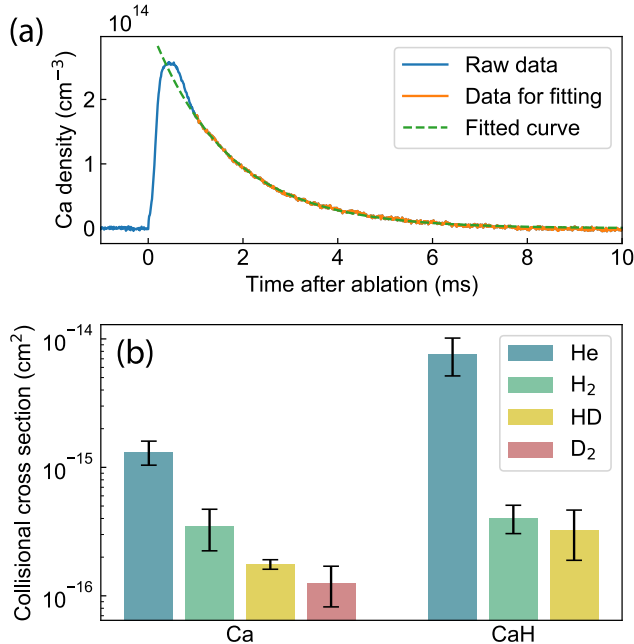


FIG. 4. (a) Sample Ca density trace as a function of time after the ablation pulse. The blue curve is the original data, the orange line highlights the data used for fitting, and the green dashed line indicates the fitted result. This data is obtained with 8.8 SCCM He flow. (b) Measured collisional cross sections of He, H₂, HD, and D₂ with Ca and CaH.

We employ a method adapted from Ref. [24], where we monitor the exponential decays of in-cell signals over time to derive the elastic collisional cross section. Details of the method can be found in Appendix D. The data is presented in Fig. 4.

In order to reduce measurement errors, we select multiple ablation spot and flow rate combinations, and take statistical averages of the results. Given the low densities of Ca and CaH (or CaD) when using the HD and D₂ gases, we average these measurements more extensively. Noticeable shifts in the background signal were observed during measurements involving H₂, HD, and D₂, likely due to sublimation of ice deposits on the cell windows. This was accounted for by including a constant offset in the exponential fit. Ultimately, we have measured the elastic cross section of H₂ with CaH to be $4.1(1.0) \times 10^{-16}$ cm². This is high enough for efficient translational cooling in a regular buffer gas cell. We have also mea-

sured the ro-vibrational temperature of CaH with a H₂ buffer gas (Appendix A) which provided evidence for efficient cooling with H₂.

IV. DISCUSSION

We have observed and quantified the remarkable chemical and thermal properties of H₂ molecules as a reactant and buffer gas in CBGB sources. Our study of the chemical production of CaH molecules demonstrates several notable phenomena that broaden the scope of cryogenic chemistry studies. This work also demonstrates a reliable method for generating cold CaH molecules in their ro-vibrational ground states, which shows a ~ 5 -fold improvement over previous approaches [42–44], and holds significant promise for producing ultracold trapped clouds of CaH and ultimately H atoms for quantum chemistry experiments and high-precision spectroscopy [45].

The successful production of CaH molecules despite the significant reaction barrier (~ 2.7 eV) demonstrates the effectiveness of H₂ as both a reactant and a cooling agent. This observation challenges the conventional thermodynamic assumptions associated with endothermic reactions in CBGB setups. The ability of H₂ to simultaneously facilitate chemical reactions and act as a buffer gas coolant highlights a dual functionality that has not been previously explored in depth.

The isotopic comparison reveals that H₂ outperforms D₂ and HD in both chemical reactivity and buffer gas cooling efficiency. This disparity can be attributed to the higher saturated vapor pressure and lower melting point of H₂ at cryogenic temperatures, as well as larger collisional cross-sections. These properties ensure a more robust supply of cold H₂ molecules in the gas phase.

We have simulated the reaction dynamics in a CBGB source using a reaction network model supplied with reaction rates from QCT simulations. This reaction model predicts the dependence of the reaction rate on the vibrational state of H₂ and successfully captures several qualitative trends observed in our experiments. This includes the influence of translational temperature on reaction dynamics and the isotopic differences. However, the inability of the model to accurately predict the reaction efficiency trend in the high density regime points to the need for more refined theoretical approaches such as including additional quantum mechanical effects.

This study advances the understanding of cryogenic chemical reactions and highlights the potential of H₂ as a versatile tool in CBGB systems. By combining experimental observations with computational modeling, we provide a comprehensive picture of the unique properties of H₂ and its isotopologues, paving the way for future explorations in this field.

V. ACKNOWLEDGMENTS

This work was supported by the AFOSR MURI Grant No. FA9550-21-1-0069 and ONR Grant No. N00014-21-1-2644, and we acknowledge generous support by the Brown Science

Foundation. R. K. and J. P.-R. acknowledge support by the AFOSR Grant No. FA9550-23-1-0202.

APPENDIX A: ROTATIONAL TEMPERATURE MEASUREMENT

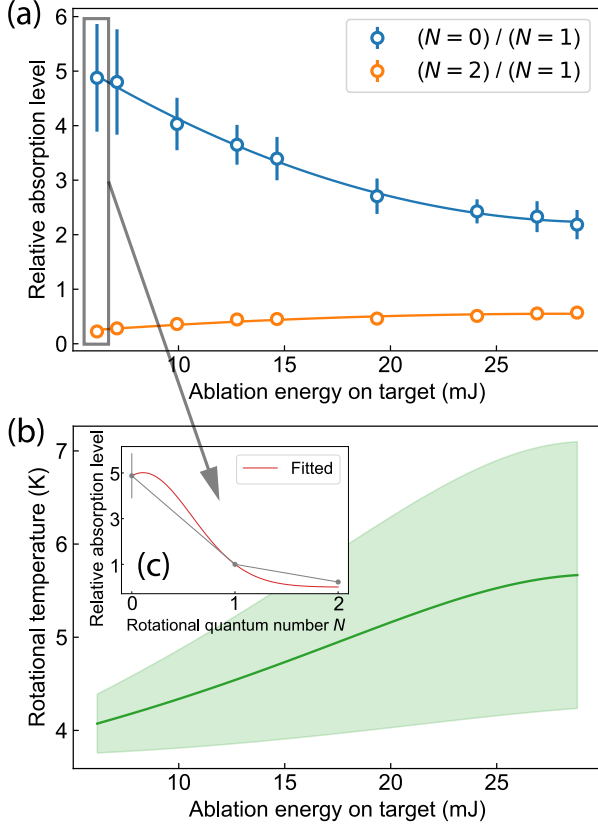


FIG. 5. (a) Relative in-cell absorption for $X^2\Sigma^+(N=0)$ and $X^2\Sigma^+(N=2)$ states with respect to $X^2\Sigma^+(N=1)$, versus ablation energy. Absorption for $X^2\Sigma^+(N=3)$ and higher ro-vibronic states is below the detection limit and therefore neglected. Solid lines are fitted quadratic functions to guide the eyes. (b) Fitted rotational temperature versus ablation energy. Temperatures are extracted from a least-squares fit according to Eq. (A1), as shown in inset (c).

We measure the rotational temperature of the molecules by comparing the relative populations in different rotational states. Figure 5(a) shows the measured relative absorption of $X^2\Sigma^+(N=0)$ and $X^2\Sigma^+(N=2)$ states with respect to $X^2\Sigma^+(N=1)$ for varying ablation energies. The transitions involved in these measurements are $A^2\Pi_{1/2}(v'=0, J'=1/2, -) \leftarrow X^2\Sigma^+(v''=0, N''=0, J''=1/2, +)$, $A^2\Pi_{1/2}(v'=0, J'=3/2, +) \leftarrow X^2\Sigma^+(v''=0, N''=1, J''=3/2, -)$, and $A^2\Pi_{1/2}(v'=0, J'=5/2, -) \leftarrow X^2\Sigma^+(v''=0, N''=2, J''=5/2, +)$, for the states with $N=0, 1$, and 2 , respectively. We fit the relative absorption values to extract the corresponding rotational temperature via the expression

$$P \propto S \times d \times e^{-BN(N+1)/k_B T}, \quad (\text{A1})$$

where P , S , d , and B denote the absorption, the Hönl-London factor, the degeneracy of the hyperfine states, and the ground-state rotational constant, respectively, and k_B is the Boltzmann constant. The fitted rotational temperature as a function of ablation energy is shown in Fig. 5(b), with the inset (c) showing a sample fit. With the knowledge of the rotational temperature, we can use the population in the $X^2\Sigma^+(N=1)$ state to predict the population in all occupied rotational states. We find that the rotational states higher than $X^2\Sigma^+(N=2)$ can be neglected here since their population is very small with buffer gas cooling down to ~ 6 K.

APPENDIX B: QCT SIMULATIONS

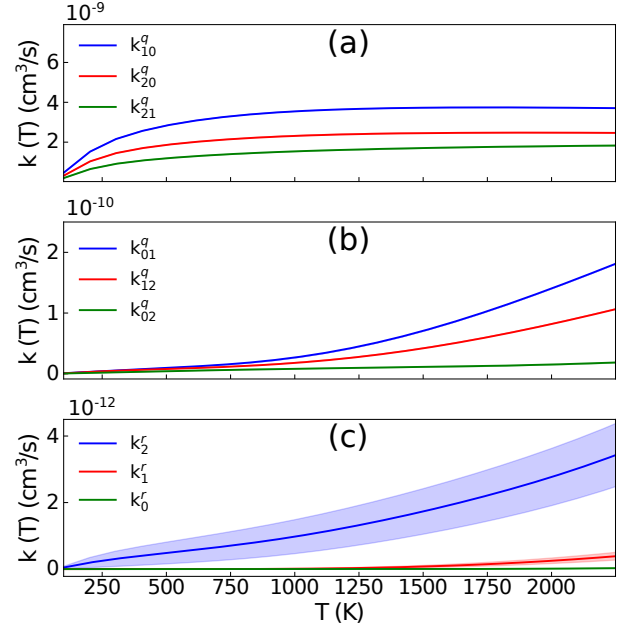


FIG. 6. Temperature-dependent rates for the (a) vibrational quenching of H₂ and (b) vibrational excitation of H₂, where the subscripts denote the initial and final vibrational states of H₂, and (c) formation of CaH from the collision between Ca and H₂, where the subscripts denote the initial vibrational state of H₂.

We use the quasi-classical trajectory method (QCT) [46, 47] via the PyQCAMS [48] software to calculate the energy-dependent cross sections relevant to the reaction network in Eqs. (1-2). The particle motion is treated classically, such that their trajectories are found using Hamilton's equations of motion. The internal states are treated according to the Bohr-Sommerfeld quantization rule, which quantizes the classical action into discrete energy levels. Thus, we gain insight into the state-to-state cross sections of relevant processes, such as the vibrational excitation or quenching of H₂, or a reaction leading to CaH formation, at variable collision energies. For an appropriate Maxwell-Boltzmann distribution of energies, we then calculate the temperature-dependent rates of these processes by integrating the cross sections over the energy

range. For example, after calculating the energy-dependent cross section $\sigma_{ij}^q(E)$ of a vibrational excitation of H_2 from state i to state j through collisions with Ca, the temperature-dependent rate is given by

$$k_{ij}^q(T) = \frac{2}{(k_B T)^{3/2}} \int \sigma_{ij}^q(E) v(E) \sqrt{\frac{E}{\pi}} e^{-E/k_B T} dE, \quad (\text{B1})$$

where $v(E) = \left(\frac{2E}{\mu}\right)^{1/2}$ represents the relative velocity between Ca and H_2 , with the reduced mass $\mu = m_{\text{Ca}} m_{\text{H}_2} / (m_{\text{Ca}} + m_{\text{H}_2})$. The same procedure is performed to calculate the temperature-dependent rate for reactive collisions leading to CaH formation, $k_i^r(T)$, for a given initial vibrational state i of H_2 . Figure 6 presents the temperature-dependent rates that were used in our reaction model.

APPENDIX C: ABLATION PLUME TEMPERATURE MEASUREMENT

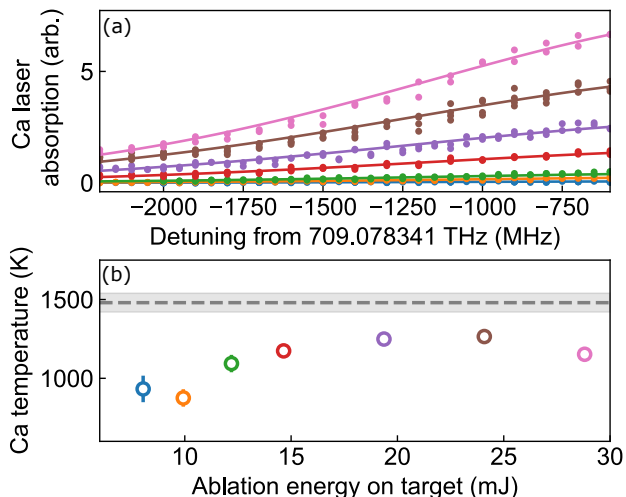


FIG. 7. (a) Ca absorption spectra at different ablation energies. The data is fitted with the Gaussian function. (b) The Ca plume temperature versus ablation energy. The gray shaded area represents the theoretical temperature that optimally matches with experimental results in the main panel of Fig. 2.

We have measured the dependence of the ablation plume temperature on the ablation energy when there is no gas flow in the system, as shown in Fig. 7. The temperature of the ablation plume is determined by analyzing the measured absorption linewidth of the Ca $4s4p \ ^1P_1 \leftarrow 4s^2 \ ^1S_0$ transition at 423 nm. While the Ca yield remains stable during the measurement, we sweep the frequency of the 423 nm laser through the cell and observe a Gaussian-shaped absorption spectrum. Its linewidth is influenced by various line-broadening mechanisms which we carefully consider to identify the dominant contributor.

The natural linewidth of the transition is ~ 30 MHz. Collisional broadening is negligible here due to the low density

of the buffer gas in the cell, and power broadening is minimal due to the low intensity of the probe laser light. Consequently, the dominant broadening mechanism is attributed to the Doppler effect. The measured linewidth of ~ 1 GHz is significantly larger than any of the other broadening contributions, allowing us to directly translate the linewidth to temperature.

It is important to note that the measured temperature represents a lower bound on the actual translational temperature of the ablation plume. In non-equilibrium systems such as the CBGB source, the translational temperature is anisotropic: the temperature along the direction of ablation is typically higher than the temperature perpendicular to it [49]. Based on our QCT simulations, a temperature of 1480(60) K provides the best fits to the experimental data. We therefore estimate this value to be near the average plume temperature in our system. Future experiments with more optical access could enable measurements along multiple spatial directions to provide a more precise characterization of the plume's anisotropic temperature distribution.

APPENDIX D: EXTRACTION OF COLLISIONAL CROSS SECTIONS

Here we describe the determination of the elastic collisional cross sections. These measurements are based on the method in Ref. [24]. We assume that particles either stick to the cell walls or exit through the cell aperture via a diffusion process when the density of buffer gas is low. By monitoring the decay of the signal over time, we estimate the diffusion time constant and consequently derive the elastic collisional cross section.

The diffusion time constant is extracted by fitting an exponentially decaying function to the later part of the absorption time trace as illustrated in Fig. 4(a). The elastic collisional cross section is then

$$\sigma = \frac{9\pi v_{\text{BG}} \tau}{16A_{\text{cell}} n_{\text{BG}}}, \quad (\text{D1})$$

where $v_{\text{BG}} = \sqrt{8k_B T_0 / \pi m_{\text{BG}}}$ is the expected speed of the buffer gas which follows the standard Maxwell-Boltzmann distribution, τ is the fitted diffusion time constant, A_{cell} is the cross-sectional cell area of ~ 5 cm², and n_{BG} is the density of the buffer gas. The density is set by controlling the flow as $n_{\text{BG}} = 4f_{\text{BG}} / v_{\text{BG}} A_{\text{aperture}}$, where f_{BG} is the flow rate of the buffer gas into the system and A_{aperture} is the aperture size of the buffer gas cell of ~ 0.25 cm².

TABLE I. Collisional cross sections (in units of 10^{-16} cm²) for Ca and CaH with He, H_2 , HD, and D_2 .

	He	H_2	HD	D_2
Ca	13.2(2.8)	3.5(1.2)	1.8(0.2)	1.3(0.4)
CaH	77(25)	4.1(1.0)	3.3(1.4)	–

To reduce systematic errors, we chose 3 different ablation spots and 2 different gas flow rates, and averaged the results

to obtain the cross section values and the measurement error

estimates. The results are presented in Table I.

-
- [1] A. Dalgarno, Some problems in interstellar chemistry, *International Journal of Mass Spectrometry and Ion Processes* **81**, 1 (1987).
- [2] I. W. Smith, Laboratory astrochemistry: Gas-phase processes, *Annual Review of Astronomy and Astrophysics* **49**, 29 (2011).
- [3] Y. Xie, H. Zhao, Y. Wang, Y. Huang, T. Wang, X. Xu, C. Xiao, Z. Sun, D. H. Zhang, and X. Yang, Quantum interference in $H + HD \rightarrow H_2 + D$ between direct abstraction and roaming insertion pathways, *Science* **368**, 767 (2020).
- [4] H. Son, J. J. Park, Y.-K. Lu, A. O. Jamison, T. Karman, and W. Ketterle, Control of reactive collisions by quantum interference, *Science* **375**, 1006 (2022).
- [5] Y.-X. Liu, L. Zhu, J. Luke, J. J. A. Houwman, M. C. Babin, M.-G. Hu, and K.-K. Ni, Quantum interference in atom-exchange reactions, *Science* **384**, 1117 (2024).
- [6] Y. T. Lee, Molecular beam studies of elementary chemical processes, *Science* **236**, 793 (1987).
- [7] J. Jankunas and A. Osterwalder, Cold and controlled molecular beams: Production and applications, *Annual Review of Physical Chemistry* **66**, 241 (2015).
- [8] W. E. Perreault, N. Mukherjee, and R. N. Zare, Supersonic beams of mixed gases: A method for studying cold collisions, *Chemical Physics* **514**, 150 (2018).
- [9] A. Kilaj, H. Gao, D. Rösch, U. Rivero, J. Küpper, and S. Willitsch, Observation of different reactivities of *para* and *ortho*-water towards trapped diazenylium ions, *Nature Communications* **9**, 2096 (2018).
- [10] S. Y. T. van de Meerakker, H. L. Bethlem, N. Vanhaecke, and G. Meijer, Manipulation and control of molecular beams, *Chemical Reviews* **112**, 4828 (2012).
- [11] H. L. Bethlem, G. Berden, and G. Meijer, Decelerating neutral dipolar molecules, *Phys. Rev. Lett.* **83**, 1558 (1999).
- [12] J. Jankunas and A. Osterwalder, Cold and controlled molecular beams: Production and applications, *Annual Review of Physical Chemistry* **66**, 241 (2015).
- [13] X. Wu, T. Gantner, M. Koller, M. Zeppenfeld, S. Chervakov, and G. Rempe, A cryofuge for cold-collision experiments with slow polar molecules, *Science* **358**, 645 (2017).
- [14] F. B. V. Martins, V. Zhelyazkova, A. Osterwalder, and F. Merkt, Cold ion-molecule chemistry: The very different reactions of He^+ with CO and NO, *CHIMIA* **77**, 221 (2023).
- [15] B. Margulis, K. P. Horn, D. M. Reich, M. Upadhyay, N. Kahn, A. Christianen, A. van der Avoird, G. C. Groenenboom, M. Meuwly, C. P. Koch, and E. Narevicius, Tomography of Feshbach resonance states, *Science* **380**, 77 (2023).
- [16] P. F. Staunum, K. Højbjerg, P. S. Skyt, A. K. Hansen, and M. Drewsen, Rotational laser cooling of vibrationally and translationally cold molecular ions, *Nature Physics* **6**, 271 (2010).
- [17] L. Xu, J. Toscano, and S. Willitsch, Trapping and sympathetic cooling of conformationally selected molecular ions, *Phys. Rev. Lett.* **132**, 083001 (2024).
- [18] H. Hirzler, R. S. Lous, E. Trimby, J. Pérez-Ríos, A. Safavi-Naini, and R. Gerritsma, Observation of chemical reactions between a trapped ion and ultracold Feshbach dimers, *Phys. Rev. Lett.* **128**, 103401 (2022).
- [19] M. McDonald, B. H. McGuyer, F. Apfelbeck, C.-H. Lee, I. Majewska, R. Moszynski, and T. Zelevinsky, Photodissociation of ultracold diatomic strontium molecules with quantum state control, *Nature* **534**, 122 (2016).
- [20] Y. Liu and K.-K. Ni, Bimolecular chemistry in the ultracold regime, *Annual Review of Physical Chemistry* **73**, 73 (2022).
- [21] J. L. Bohn, A. M. Rey, and J. Ye, Cold molecules: Progress in quantum engineering of chemistry and quantum matter, *Science* **357**, 1002 (2017).
- [22] S. S. Kondov, C.-H. Lee, M. McDonald, B. H. McGuyer, I. Majewska, R. Moszynski, and T. Zelevinsky, Crossover from the ultracold to the quasiclassical regime in state-selected photodissociation, *Phys. Rev. Lett.* **121**, 143401 (2018).
- [23] S. E. Maxwell, N. Brahm, R. deCarvalho, D. R. Glenn, J. S. Helton, S. V. Nguyen, D. Patterson, J. Petricka, D. DeMille, and J. M. Doyle, High-flux beam source for cold, slow atoms or molecules, *Phys. Rev. Lett.* **95**, 173201 (2005).
- [24] N. R. Hutzler, H.-I. Lu, and J. M. Doyle, The buffer gas beam: An intense, cold, and slow source for atoms and molecules, *Chem. Rev.* **112**, 4803 (2012).
- [25] M. G. Tarallo, G. Z. Iwata, and T. Zelevinsky, BaH molecular spectroscopy with relevance to laser cooling, *Phys. Rev. A* **93**, 032509 (2016).
- [26] J. L. Bohn, Molecular spin relaxation in cold atom-molecule scattering, *Phys. Rev. A* **61**, 040702 (2000).
- [27] J. Kłos, E. Tiesinga, and S. Kotochigova, Quantum scattering of icosahedron fullerene C_{60} with noble-gas atoms, *Scientific Reports* **14**, 9267 (2024).
- [28] V. Singh, K. S. Hardman, N. Tariq, M.-J. Lu, A. Ellis, M. J. Morrison, and J. D. Weinstein, Chemical reactions of atomic lithium and molecular calcium monohydride at 1 K, *Phys. Rev. Lett.* **108**, 203201 (2012).
- [29] L. Anderegg, B. L. Augenbraun, E. Chae, B. Hemmerling, N. R. Hutzler, A. Ravi, A. Collopy, J. Ye, W. Ketterle, and J. M. Doyle, Radio frequency magneto-optical trapping of CaF with high density, *Phys. Rev. Lett.* **119**, 103201 (2017).
- [30] J. Lim, J. R. Almond, M. A. Trigatzis, J. A. Devlin, N. J. Fitch, B. E. Sauer, M. R. Tarbutt, and E. A. Hinds, Laser cooled YbF molecules for measuring the electron's electric dipole moment, *Phys. Rev. Lett.* **120**, 123201 (2018).
- [31] S. C. Wright, M. Doppelbauer, S. Hofsäss, H. C. Schewe, B. Sartakov, G. Meijer, and S. Truppe, Cryogenic buffer gas beams of AlF, CaF, MgF, YbF, Al, Ca, Yb and NO - a comparison, *Molecular Physics* **121**, e2146541 (2023).
- [32] S. Truppe, S. Marx, S. Kray, M. Doppelbauer, S. Hofsäss, H. C. Schewe, N. Walter, J. Pérez-Ríos, B. G. Sartakov, and G. Meijer, Spectroscopic characterization of aluminum monofluoride with relevance to laser cooling and trapping, *Phys. Rev. A* **100**, 052513 (2019).
- [33] N. B. Vilas, C. Hallas, L. Anderegg, P. Robichaud, A. Winnicki, D. Mitra, and J. M. Doyle, Magneto-optical trapping and sub-doppler cooling of a polyatomic molecule, *Nature* **606**, 70 (2022).
- [34] B. L. Augenbraun, Z. D. Lasner, A. Frenett, H. Sawaoka, C. Miller, T. C. Steimle, and J. M. Doyle, Laser-cooled polyatomic molecules for improved electron electric dipole moment searches, *New Journal of Physics* **22**, 022003 (2020).
- [35] I. Kozyryev, L. Baum, K. Matsuda, B. L. Augenbraun, L. Anderegg, A. P. Sedlack, and J. M. Doyle, Sisyphus laser cooling of a polyatomic molecule, *Phys. Rev. Lett.* **118**, 173201 (2017).
- [36] D. Mitra, N. B. Vilas, C. Hallas, L. Anderegg, B. L. Augen-

- braun, L. Baum, C. Miller, S. Raval, and J. M. Doyle, Direct laser cooling of a symmetric top molecule, *Science* **369**, 1366 (2020).
- [37] G.-Z. Zhu, D. Mitra, B. L. Augenbraun, C. E. Dickerson, M. J. Frim, G. Lao, Z. D. Lasner, A. N. Alexandrova, W. C. Campbell, J. R. Caram, J. M. Doyle, and E. R. Hudson, Functionalizing aromatic compounds with optical cycling centres, *Nature Chemistry* **14**, 995 (2022).
- [38] X. Liu, W. Wang, S. C. Wright, M. Doppelbauer, G. Meijer, S. Truppe, and J. Pérez-Ríos, The chemistry of AlF and CaF production in buffer gas sources, *The Journal of Chemical Physics* **157**, 074305 (2022).
- [39] R. Koots, J. Dai, Q. Sun, B. Riley, D. Mitra, T. Zelevinsky, and J. Pérez-Ríos, Theoretical investigation of CaH production in buffer gas sources, manuscript in preparation (2024).
- [40] P. C. Souers, C. K. Briggs, J. W. Pyper, and R. T. Tsugawa, *Hydrogen vapor pressures from 4 to 30 K: a review*, Report (Lawrence Livermore Lab, 1977).
- [41] H. J. Hoge and R. D. Arnold, Vapor pressures of hydrogen, deuterium, and hydrogen deuteride and dew-point pressures of their mixtures, *J. Research Natl. Bur. Standards* **47**, 2 (1951).
- [42] S. F. Vázquez-Carson, Q. Sun, J. Dai, D. Mitra, and T. Zelevinsky, Direct laser cooling of calcium monohydride molecules, *New Journal of Physics* **24**, 083006 (2022).
- [43] R. McNally, I. Kozyrev, S. Vazquez-Carson, K. Wenz, T. Wang, and T. Zelevinsky, Optical cycling, radiative deflection and laser cooling of barium monohydride, *New Journal of Physics* **22**, 083047 (2020).
- [44] J. Dai, Q. Sun, B. C. Riley, D. Mitra, and T. Zelevinsky, Laser cooling of a fermionic molecule, *Phys. Rev. Res.* **6**, 033135 (2024).
- [45] Q. Sun, C. E. Dickerson, J. Dai, I. M. Pope, L. Cheng, D. Neuhauser, A. N. Alexandrova, D. Mitra, and T. Zelevinsky, Probing the limits of optical cycling in a predissociative diatomic molecule, *Phys. Rev. Res.* **5**, 043070 (2023).
- [46] D. G. Truhlar and J. T. Muckerman, Reactive scattering cross sections III: Quasiclassical and semiclassical methods, in *Atom-molecule collision theory: A guide for the experimentalist* (Plenum Press, New York, 1979) pp. 505 – 561.
- [47] J. Pérez-Ríos, Cold chemical reactions between molecular ions and neutral atoms, in *An introduction to cold and ultracold chemistry: Atoms, molecules, ions and Rydbergs* (Springer International Publishing, 2020) pp. 215 – 234.
- [48] R. Koots and J. Pérez-Ríos, Pyqcams: Python quasi-classical atom-molecule scattering, *Atoms* **12**, 5 (2024).
- [49] S. M. Skoff, R. J. Hendricks, C. D. J. Sinclair, J. J. Hudson, D. M. Segal, B. E. Sauer, E. A. Hinds, and M. R. Tarbutt, Diffusion, thermalization, and optical pumping of YbF molecules in a cold buffer-gas cell, *Phys. Rev. A* **83**, 023418 (2011).